Near-ifrared-II photodetectors based on silver selenide quantum dots on mesoporous TiO_2 scaffolds

Graddage, Neil; Ouyang, Jianying; Lu, Jianping; Chu, Ta-Ya; Zhang, Yanguang; Li, Zhao; Wu, Xiaohua; Malenfant, Patrick R. L.; Tao, Ye

Publisher's version / Version de l'éditeur:
https://doi.org/10.1021/acsanm.0c02686
ACS Applied Nano Materials, 3, 12, pp. 12209-12217, 2020-12-02

ACS APPLIED NANO MATERIALS

www.acsanm.org Article

Near-Infrared-II Photodetectors Based on Silver Selenide Quantum Dots on Mesoporous TiO_2 Scaffolds

Neil Graddage, Jianying Ouyang, Jianping Lu,* Ta-Ya Chu, Yanguang Zhang, Zhao Li, Xiaohua Wu, Patrick R. L. Malenfant, and Ye Tao*

Cite This: *ACS Appl. Nano Mater.* 2020, 3, 12209−12217 Read Online

ACCESS | Metrics & More | Article Recommendations | Supporting Information

ABSTRACT: Biosensing applications are driving an increase in demand for low-cost photodetectors with sensitivity between 1000 and 1400 nm. Recently, the sensitivity of Ag_2Se colloidal quantum dot based devices in this wavelength range has been observed. In this work we make the first demonstration of an Ag_2Se photodiode device with sensitivity in this entire range. By employing secondary phosphine to elevate the precursor reactivity, we achieved accurate size control of the Ag_2Se nanocrystals with a distinct excitonic absorption peak. These nanocrystals were deposited from solution into a mesoporous TiO_2 scaffold, similar to that used in dye-sensitized solar cells, to increase the light absorption and charge separation and reduce the exciton diffusion length. By incorporation of a suitable hole-transporting layer between the active layer and Ag anode, the resulting devices showed a responsivity of 4.17 mA/W at a wavelength of 1200 nm. These results demonstrate that Ag_2Se colloidal quantum dots offer a low-toxicity route for low-cost fabrication of near-infrared photodetectors.

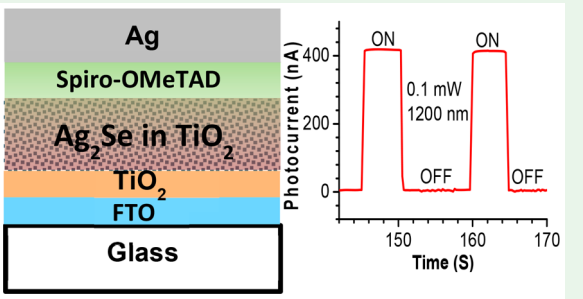

KEYWORDS: *photodetectors, second near-infrared window, Ag_2Se colloidal quantum dots, mesoporous TiO_2 scaffold, solution processing, photodiode structures*

INTRODUCTION

There is a growing need for photodetectors with sensitivity in the second near-infrared window of the electromagnetic spectrum (NIR-II, 1000−1400 nm). Because of the absorption sensitivity to molecular structure of material in this region and the capability of NIR radiation to penetrate deep biotissue, a myriad of applications in sensing and healthcare have been proposed and demonstrated.[1−3] Traditional NIR-II detection devices are based on epitaxial semiconductor heterostructures (such as InGaAs),[4] which perform well but are limited in form factor and high in cost due to the manufacturing processes required. If such devices could be fabricated by using solution processing techniques, a broad spectrum of novel device shapes, sizes, and applications would be enabled at lower cost. However, to do so, alternative materials and device structures are required.

Many alternative materials are currently under investigation for these applications, including colloidal quantum dots (CQDs).[5] These materials consist of nanosized crystalline structures of semiconductor materials and can be grown in solution, potentially enabling the use of solution processing techniques for the fabrication of devices. Such techniques could allow lower cost fabrication onto a wide variety of substrates, permitting novel devices. In particular, PbS and HgTe CQDs have demonstrated high performance, comparable to epitaxially grown InGaAs.[6−11] Because of toxicology concerns over the use of heavy metals (Pb, Hg, or Cd), research efforts have been directed toward more environmentally benign alternatives which would result in safer device manufacturing and disposal. Recently, the use of silver chalcogenide quantum dots has shown promise for NIR photodetection. Initial work focused on Ag_2Te, based on the results of Urban and co-workers,[12] who demonstrated size-dependent absorption in the NIR region. This inspired investigation into other silver chalcogenides, with Yarema et al.[13] also demonstrating NIR absorption from Ag_2Se nanocrystals. However, size-dependent absorption results in challenges for quantum dot synthesis, as ideally a narrow size distribution of CQDs should be synthesized.

To take advantage of the properties of these Ag_2Se quantum dots, various device architectures can be utilized. Even mid-infrared photodetectors have been realized by exploiting the photoexcited electron intraband transitions in Ag_2Se nanocrystals.[14−16] Hafiz et al. demonstrated the fabrication of Ag_2Se quantum dot-based NIR photodetectors with a photo-

Received: October 5, 2020
Accepted: November 23, 2020
Published: December 2, 2020

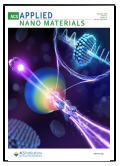

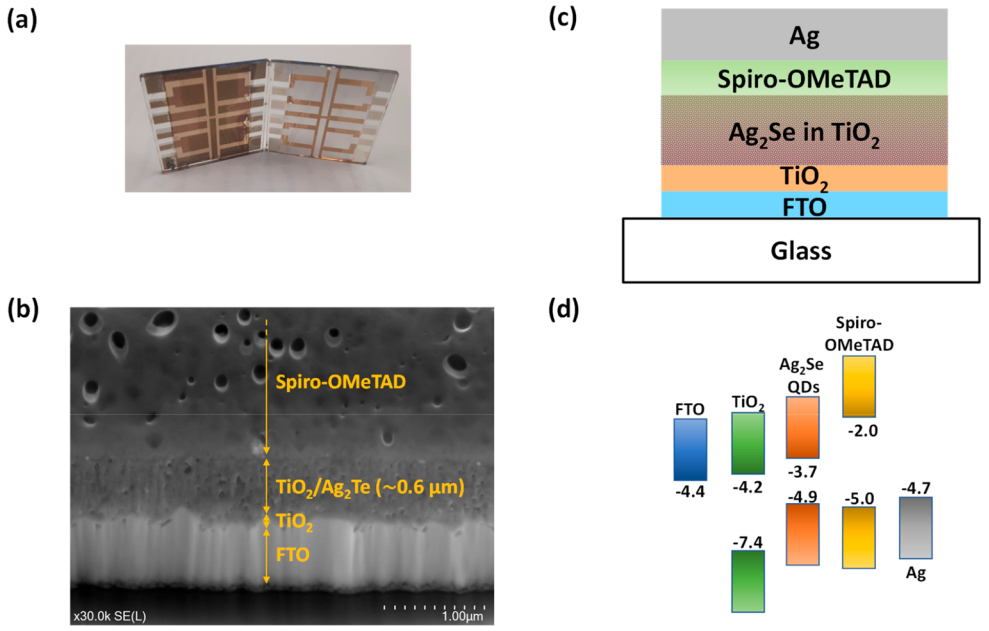

Figure 1. (a) Photograph of fabricated devices. (b) SEM image of device (without Ag electrode), showing the thickness of the mesoporous TiO_2 layer to be 580 nm. (c) Schematic showing device structure. (d) Energy diagram of device. The Ag_2Se bandgap was calculated from optical absorption measurements; all other values are from the literature.

conductor structure;[15] however, the responsivity observed was poor, which they attributed to low carrier concentration as a result of their use of 1,2-ethanedithiol for ligand exchange. Lee et al.[17] demonstrated similar devices on a flexible substrate, showing the potential for low-temperature processing. Photoconductor structures are relatively simple to produce and can enable high quantum efficiency, but at the expense of increased dark current and power consumption,[18] significant factors for many applications. The responsivity of photoconductor devices depends on the photoconductive gain achieved by the long carrier lifetime. Unfortunately, this severely limits the device speed; therefore, there is a trade-off between sensitivity and speed for photoconductor-based photodetectors.[19] Photodiode structures are similar in mechanism to solar cells and can operate without external power. The use of Ag_2Se quantum dots in solar cell applications has been demonstrated, including in dye-sensitized solar cells (DSSCs) as a blocking layer.[20] The DSSC structure has also been demonstrated for IR photodetection using $CuInSe_2$ quantum dots by Guo et al.,[21] who achieved broadband photodetection (300−1100 nm) by using Spiro-OMeTAD as both a hole-transport layer and a UV absorber, as is common in solid-state DSSCs.[22] The $CuInSe_2$ quantum dots infiltrate the mesoporous TiO_2 structure, allowing exploitation of the large surface area to volume ratio of the quantum dots and reducing the exciton diffusion length.

In this work we report on an NIR photodetector based upon Ag_2Se quantum dots in a mesoporous TiO_2 scaffold. Accurate size control of Ag_2Se quantum dots was achieved by employing secondary phosphine to elevate the precursor reactivity, resulting in well-defined absorption peaks. These quantum dots were then processed from solution into a mesoporous TiO_2 layer for integration into a photodiode which demonstrated broad sensitivity up to 1400 nm, way beyond the detection limit of Si photodetectors (1100 nm, without defect engineering[23]). The device structure is shown in Figure 1. Under 1 mW irradiation at 1200 nm, a photocurrent of 4.17 μA was obtained, showing an on/off ratio as high as 490.

RESULTS AND DISCUSSION

Ag_2Se Colloidal Quantum Dot Synthesis and Characterization. In the past decade a number of literature reports have emerged about the synthesis of colloidal Ag_2Se QDs, including various silver sources such as silver trifluoroacetate, silver nitrate, silver chloride, and silver acetate (AgAc), various ligands such as oleylamine, oleic acid, tetradecylphosphonic acid, 1-octanethiol, and 1-dodecanethiol (DDT), and various selenium sources such as elemental selenium and tri-*n*-octylphosphine selenide (TOPSe).[13,24−27] Typically, these Ag_2Se CQD syntheses employed a hot injection method, wherein one source (either Ag or Se) was swiftly injected into a flask containing another source at elevated temperature, and the growth was quenched after a certain period of time. We employed AgAc, DDT, and TOPSe as well as the noncoordinating solvent 1-octadecene (ODE) for the following reasons: DDT is a strong ligand toward Ag, facilitating the control of crystal nucleation and growth; TOPSe is a relatively stable precursor of Se, and more importantly secondary phosphine can be applied by Se exchange to drastically increase and tune the Se reactivity;[28−34] and ODE is an environmentally benign solvent and does not participate in the reaction, thus simplifying the reaction system. Briefly, AgAc, DDT, and ODE were degassed at 70 °C under vacuum (50 mTorr) for 90 min, followed by a swift injection of TOPSe containing diphenylphosphine (DPP) under high-purity nitrogen at 140 °C. The temperature was dropped to ∼130 °C after injection, and the growth was maintained at 120 °C for 60 min (starting from the injection). The crude reaction product was dispersed in toluene, precipitated by anhydrous ethanol, and then centrifuged. To the best of our knowledge, we are the first to introduce secondary phosphine to the synthesis of colloidal Ag_2Se QDs and have achieved tunable size with a narrow size distribution.[35] Figure 2 compares the optical properties of Ag_2Se QDs with versus without DPP. In the presence of DPP (a), nucleation occurred instantly with a high concentration of nuclei, followed by rapid size growth and focus in 10 min;

https://dx.doi.org/10.1021/acsanm.0c02686
ACS Appl. Nano Mater. 2020, 3, 12209−12217

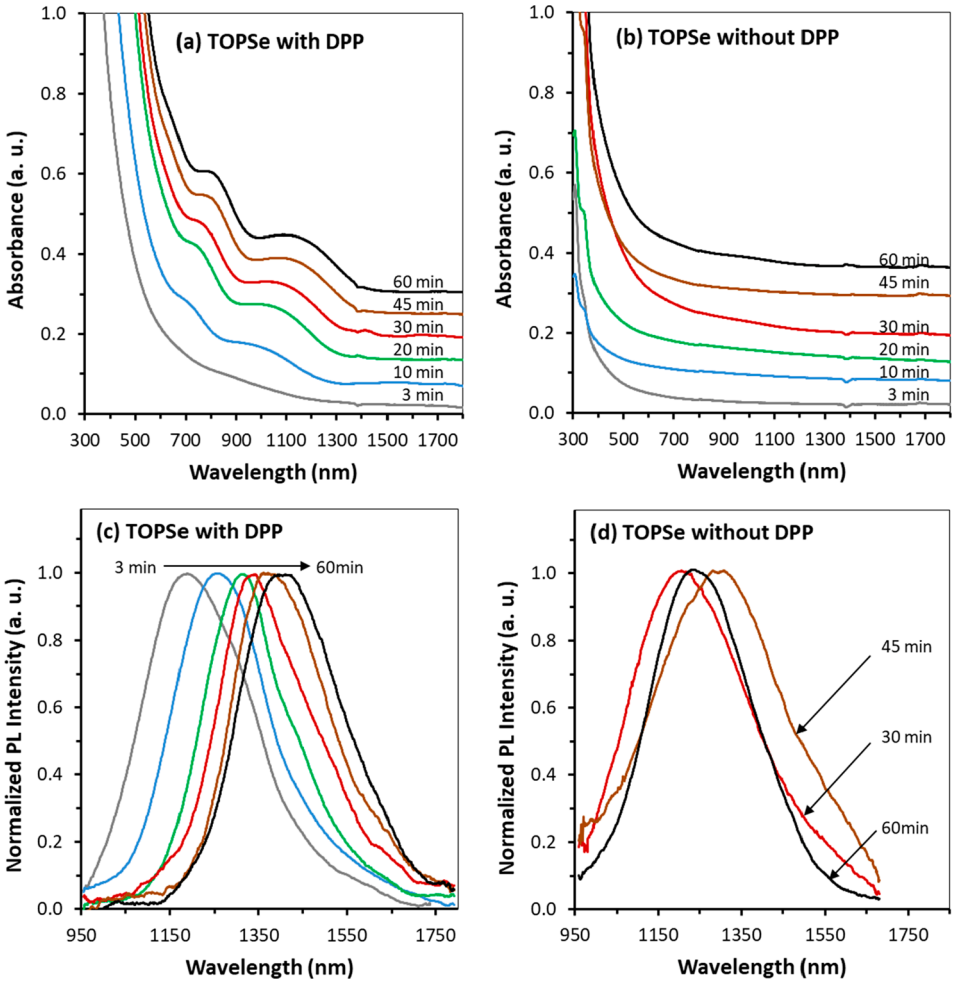

Figure 2. Temporal evolution of optical properties of growing Ag_2Se QDs with and without diphenylphosphine (DPP): absorption spectra (offset for clarity, optical path 4 mm) with DPP (a) and without DPP (b), the growth times (3, 10, 20, 30, 45, and 60 min) are indicated; the corresponding PL emission spectra (normalized) with DPP (c) and without DPP (d). The absorption spectra were normalized to 0.25 g of crude growth mixtures sampled and dispersed in 1.0 mL of TCE. The PL emission spectra were excited at 917 nm, except the 3 min growth sample in (c), which was excited at 882 nm instead. Diluted samples were used with optical density around 0.1 at the excitation wavelength for PL emission measurement.

afterward, the size kept increasing in a steady manner with the absorption peak shifting from ~950 to ~1150 nm in 1 h monitored. In contrast, in the absence of DPP (b), nucleation occurred with a very low concentration of nuclei, and the growth was slow with no distinctive features in the absorption spectra. The corresponding photoluminescence (PL) emission spectra in the presence of DPP (c) exhibited peak shifting from ~1200 to 1400 nm, but the PL quantum yield (QY) decreased from 5.4% for the 3 min growth sample to 2.7%, 1.3%, 1.2%, 0.9%, and 0.7% for 10, 20, 30, 45, and 60 min growth samples, respectively, suggesting fast growth did not benefit the QD surface perfection and passivation. The corresponding PL emission spectra in the absence of DPP (d) exhibited a peak in the range ~1220—1320 nm, and the PL QY increased from 1.1% for the 30 min growth sample to 1.5% and 1.8% for 45 and 60 min growth samples, respectively, suggesting slow growth facilitates the QD surface perfection and passivation. Overall, the presence of DPP greatly promoted the Ag_2Se nuclei concentration thanks to elevated precursor reactivity, sped up the nanocrystal growth, and led to size focus in a short period of time. However, the PL QY decreased with the reaction time, probably due to overfast growth.

Figure 3 illustrates the purified product (from a 13-fold scale synthesis and with five-round purification) absorption spectrum and corresponding photoluminescence (PL) emission spectrum (a), size/size distribution (b), composition (c), and crystal structure (d). The absorption spectrum (black curve) exhibits distinct fine features with the first excitonic peak at ~1070 nm, and the PL emission (red curve) exhibits a peak at 1327 nm, with the Stokes shift (the energy difference between the peak positions of the first excitonic absorption and the PL emission peak) being 218.0 meV. The large Stokes shift suggests the existence of a trap state beside the intrinsic state, which has been observed in other Ag_2Se QDs.[36] The PL QY was determined to be ~2%. The TEM image shows nanocrystals with a mean size of 3.7 ± 1.1 nm from statistics on ~200 nanocrystals (see the histogram in Figure S1 of the Supporting Information), and the inset shows a nanocrystal with clear crystal fringes (see more TEM images in Figure S1). EDX analysis confirms the product is silver selenide with mean atomic percentages of Ag 61.70% and Se 20.12% (see Scheme S1a for all measurements). The ~3:1 Ag/Se atomic ratio is higher than the stoichiometric ratio 2:1, indicating that the surface is highly rich in Ag, which facilitates the coordination

https://dx.doi.org/10.1021/acsanm.0c02686
ACS Appl. Nano Mater. 2020, 3, 12209−12217

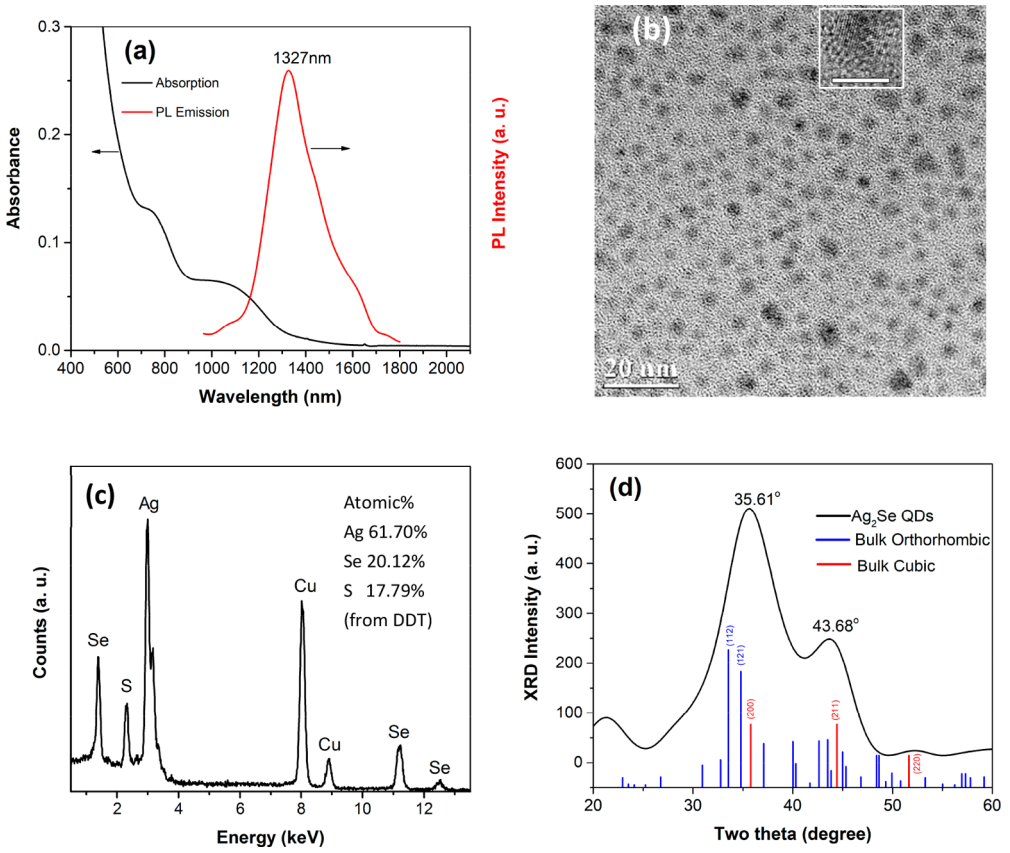

Figure 3. Characteristics of the purified Ag_2Se QDs. (a) Absorption (black) and photoluminescence (PL) emission (red, excited at 917 nm) spectra. (b) TEM image (20 nm scale bar), with the inset showing crystal fringes (scale bar 5 nm). (c) EDX spectrum, with the inset showing atomic percentages of Ag, Se, and S (from DDT ligands). (d) XRD spectrum (black), with spectra of bulk orthorhombic (blue) and bulk cubic (red) included as references.

to ligands so that the surface is better protected.[27] On the other hand, sulfur was detected to be 17.79%, which should be from DDT ligands, as seen previously in octanethiol-capped Ag_2Se QDs.[26] Interestingly, P was detected by EDX to be only 0.38%, indicating negligible coverage by the relatively weak ligand TOP, which was also observed in stearic acid-capped CdSe QDs.[37] The Ag_2Se QDs lose ~30% weight from 195 to 300 °C as determined by thermogravimetric analysis (TGA) (see Scheme S1b); i.e., the surface ligands occupy ~30% weight, corresponding to a ligand density of 6.5/nm^2 (see detailed calculation in Scheme S1c). Fisher et al. reported 2.3 ligand (stearic acid)/nm^2 on the surface of 3.0 nm in diameter CdSe QDs calculated from 1D proton NMR spectrum acquired by the magic angle spinning technique, and ~29% coverage (ligand per atom) was estimated.[37] Therefore, the seemingly high sulfur content in our Ag_2Se QDS arises from the high DDT coverage on Ag_2Se QD surface. The Fourier transform infrared (FT-IR) spectrum also confirms the presence of a large amount of DDT in the purified Ag_2Se nanocrystals (Figure S2). In fact, Ag_2S or Ag−Se−S ternary QDs were not likely formed in our syntheses because Ag(I) can be effectively stabilized by DDT under 180 °C.[26] The XRD spectrum exhibits multiple peaks, with the most intense peak at 35.61°, followed by 43.68°. It is difficult to determine the crystal structure due to peak broadening caused by small crystal size (Scherrer broadening). However, the high-temperature cubic crystal structure can be excluded when the spectrum is compared with that of bulk cubic (red at the bottom, JCPDS No. 27-0619) judging by the peak intensity ratios. Because our Ag_2Se nanocrystals are of small size (3.7 nm), the low-temperature metastable tetragonal crystal structure is highly possible according to the size- and temperature-dependent phase diagram reported by Sahu et al., in which the upper boundary is ~40 nm at room temperature for Ag_2Se nanocrystals to exist in tetragonal phase.[38] In addition, the most intense peak in our spectrum at 35.61° is closer to that of tetragonal phase (35.74° and 36.20°) compared to that of orthorhombic phase (33.45° and 34.70°, blue at the bottom, JCPDS No. 24-1041).[39] Furthermore, crystals were found in the high-resolution TEM (Figure S1) with a *d*-spacing of 2.36 Å, which exists in the tetragonal phase (corresponding to (102) and (300) planes) but not in the orthorhombic phase.[24,39]

Ag_2Se exhibits different crystal structures, depending on growth conditions and temperature. The high-temperature cubic phase α-Ag_2Se is a superionic conductor used as solid electrolyte in photochargable batteries,[40] while low-temperature orthorhombic β-phase and metastable tetragonal phase Ag_2Se have emerged as promising candidates for NIR-II sensors. We optimized the nanocrystal synthesis conditions and obtained tetragonal phase Ag_2Se QDs. Bulk tetragonal phase Ag_2Se has a low bandgap of 0.07 eV, whereas bulk orthorhombic phase Ag_2Se has a bandgap of 0.15 eV.[15] The bandgap of the QDs synthesized in this report was calculated from optical absorption measurements to be 1.16 eV due to the quantum confinement. To enhance the light absorption in the NIR-II region while maintaining good dispersity in organic

https://dx.doi.org/10.1021/acsanm.0c02686
ACS Appl. Nano Mater. 2020, 3, 12209−12217

solvents for solution processing, the target CQD size was ~4 nm.

Photodetector Device Fabrication and Characteristics. To fabricate devices from solution, a suitable process for depositing optimal thickness films of the Ag_2Se CQDs had to be found. 1,2-Ethanedithiol has been used as the cross-linker for Ag_2Se QDs in the literature;[15] however, we found that this compound is odorous and difficult to handle. In our previous work we demonstrated that 1,3-benzenedithiol (BDT) can be employed as a cross-linker to replace oleic acid ligands and bridge the CQDs.[41] In this work, we found that BDT can also effectively replace 1-dodecanethiol ligands. When BDT was used for ligand exchange with our Ag_2Se CQDs, XPS analysis (see Figure S3) showed that the atomic ratio of C to Ag significantly decreased from 15.3 before to 2.2 afterward. As can be seen from the XPS results, the decrease in the C content after ligand exchange is significant. Note that both Se and S signals are weak and overlap with other elements, so it is difficult to estimate their contents from the XPS analysis. In addition, 95% of the XPS signal comes from within 5 nm of the surface or less. Considering the size of the Ag_2Se QDs (3.7 nm), the length of the DDT ligand (>1.4 nm), and the adventitious carbon from the wet process, the C content may be overestimated. Importantly, after ligand exchange, the QDs were cross-linked and became insoluble in organic solvents, which allowed for the buildup of the active layer by the layer-by-layer process. The absorption spectrum of a BDT cross-linked Ag_2Se QD film is shown in Figure S4.

Initially, to evaluate the performance of Ag_2Se QDs in NIR-II photodetectors, simple Schottky-type photodiodes with a structure of ITO/Ag_2Se QDs/LiF/Al were fabricated. Unfortunately, the devices were shorted with no diode behavior observed due to the high conductivity of the active layer (~2.4×10^{-4} S/cm from the four-probe measurement). This was initially surprising; however, we believe that the high conductivity is due to an excess of Ag^+ cations in the material, as observed by Qu et al.[14] Additionally, a high electrical conductivity of 7.6×10^2 S/cm at room temperature has been reported for 16 nm Ag_2Se QDs with an Ag/Se ratio of 2.2 ± 0.1 in the literature.[42]

To avoid device shorting and to maximize the light absorption and charge separation, a solid-state DSSC structure of FTO/compact TiO_2/Ag_2Se QD infiltrated mesoporous TiO_2/Spiro-OMeTAD/Ag was employed. The compact TiO_2 layer helps prevent shorting between electrodes while the mesoporous layer provides a scaffold for the Ag_2Se QDs. Photographs of example devices, an SEM cross section, and a schematic diagram of the device structure are shown in Figure 1. Such a device structure was demonstrated by Guo et al.[21] using $CuInSe_2$ CQDs; however, the performance in the NIR region was poor. Spiro-OMeTAD (doped with *tert*-butylpyridine and Li-TFSI, as is common in the literature[43]) was chosen as a hole-transporting layer (HTL) in our study because its HOMO energy level (−5.0 eV)[44] is a good match for the valence band of Ag_2Se QDs (−4.86 eV),[14,39] as illustrated in Figure 1d.

In a typical DSSC, a monomer layer of ruthenium complex anchored to the TiO_2 surface is enough for sunlight harvesting. However, it was found that our devices required many layers of Ag_2Se QDs coated onto the mesoporous TiO_2 in order for the devices to be functional. For example, devices with eight coatings of Ag_2Se QDs were shorted and did not show diode behavior. Devices with 17 coatings of Ag_2Se QDs (each cross-linked with BDT) were fabricated to ensure that TiO_2 was fully permeated by the QDs and that no short was possible between the electrodes. Increasing the number of Ag_2Se depositions also improves the absorption characteristics of the device. The active area of the fabricated photodetectors was 0.49 cm^2.

For comparison purposes devices were fabricated with and without the Spiro-OMeTAD HTL. As can be seen from Figure 4, the HTL significantly improved the device performance.

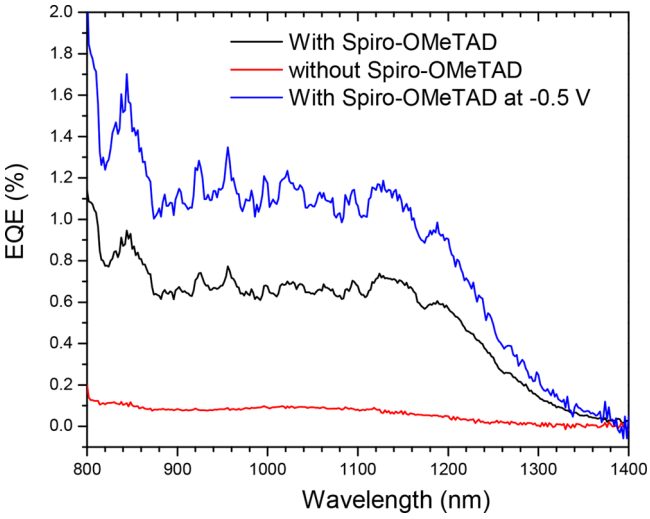

Figure 4. External quantum efficiency of Ag_2Se QDs photodetectors in the NIR-II region.

The external quantum efficiency (EQE) increased by 7 times on average in the NIR region (800−1200 nm). For example, by addition of the doped Spiro-OMeTAD layer the EQE at 1100 nm increased from 0.08% to above 0.6%. It is worth pointing out that the EQE increased further by ~50% when a reverse bias as small as −0.5 V was applied to the devices, reaching more than 1%.

Figure 5 shows the $I-V$ curves of the photodetectors in the dark and under simulated AM 1.5G irradiation of 100 mW/cm^2. Both devices showed excellent diode behavior in the dark. At −0.5 V, both devices had a low leakage current of ~7 μA/cm^2. However, when a forward bias (0.5 V) was applied, the current increased dramatically. The device with Spiro-OMeTAD HTL exhibited a turn-on current of 0.46 mA/cm^2 compared to 7.1 mA/cm^2 without. The lack of HTL results in a large on-current because of the following reasons: (i) the hole injection barrier between Spiro-OMeTAD (HOMO: −5.0 eV) and Ag (work function: −4.7 eV) was larger than that between Ag_2Se QDs (valence band: − 4.86 eV) and Ag; (ii) the electrical conductivity of cross-linked Ag_2Se QDs (2.4×10^{-4} S/cm) was much higher than that of LiTFSI-doped Spiro-OMeTAD (4×10^{-5} S/cm);[45] and (iii) the addition of the HTL increases the total thickness of the semiconductor layer. Under 1 sun irradiation, the device with a HTL delivered a short-circuit current of 0.44 mA/cm^2 and an open-circuit voltage (V_{OC}) of 0.22 V. In sharp contrast, without a HTL the device only showed a short-circuit current of 0.23 mA/cm^2 and a tiny V_{OC} of 0.04 V. This highlights the need for a suitable HTL layer to ensure efficient charge collection, as without the p-doped Spiro-OMeTAD the device is a poor Schottky junction. As expected from the literature, the Ag_2Se QDs are a good photoconductor. Both devices exhibited a significant current increase at 0.5 V under 1 sun irradiation.

https://dx.doi.org/10.1021/acsanm.0c02686
ACS Appl. Nano Mater. 2020, 3, 12209−12217

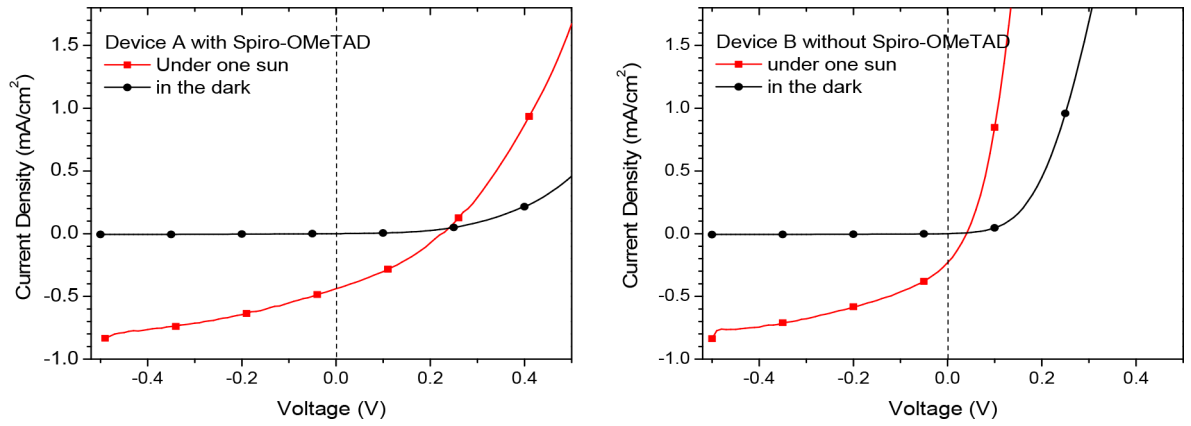

Figure 5. *I*–*V* curves of the devices with and without the HTL in the dark and under 1 sun irradiation.

Further characterization of the device with a HTL was performed to investigate device performance and stability. After exposure to air for a week, the device was tested under 1200 nm laser irradiation. As can be seen from Figure 6, the

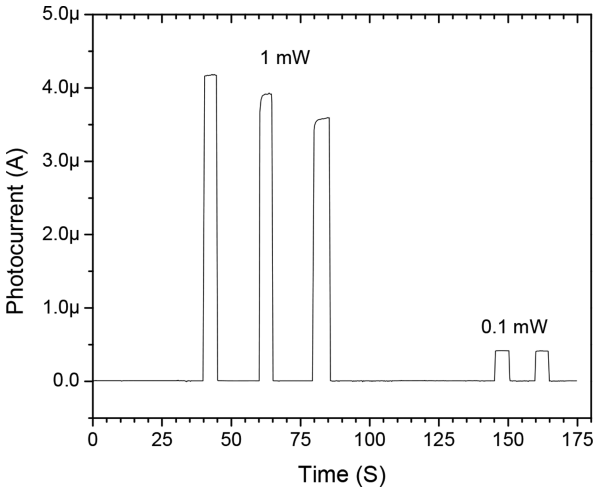

Figure 6. Photocurrent–time response of the photodetector based on Ag_2Se QDs in mesoporous TiO_2 under 1200 nm NIR irradiation at different intensities.

device shows a decent responsivity (R) of 4.17 mA/W at 1200 nm under both 1 and 0.1 mW laser irradiation. This performance was much better than comparable $CuInSe_2$ CQD-based photodetectors.[21] It is interesting to point out that a decent photocurrent of 4.17 μA was obtained under 1 mW irradiation at 1200 nm, showing an on/off ratio as high as 490. For comparison, Ag_2Se QDs photoconductor-based IR detectors only showed a moderate on/off ratio of 7.5 under 4 mW/cm^2 irradiation.[13] The rise time of our photodetectors defined as the increase in the photocurrent from 10% to 90% of the peak value was 0.21 s, and the decay time defined as the decrease in the photocurrent from 90% to 10% of the peak value was 0.24 s. Note that because of the low temporal resolution of our characterization setup, the response time of the photodiode detectors could be shorter. Device performance is higher than that reported for Ag_2Se CQDs photoconductor-based photodetectors because of the significant reduction in dark current and higher on/off ratio.[17] The performance also compares favorably to the $CuInSe_2$ devices reported by Guo et al.,[21] although they only reported behavior up to 1100 nm.

CONCLUSIONS

We demonstrated the effectiveness of using a mesoporous TiO_2 scaffold in Ag_2Se-based NIR-II photodetector structure, which helped to increase the light absorption and charge separation as well as reduce the exciton diffusion length. We also reported a novel synthesis method for Ag_2Se CQDs, resulting in accurate size control. By employing secondary phosphine to elevate the precursor reactivity, we achieved nanocrystals of mean diameter 3.7 nm with a good yield. Integration of these CQDs into a mesoporous TiO_2 scaffold with a doped Spiro-OMeTAD HTL, inspired by solid-state DSSCs, enabled photodiodes with an EQE of over 1% at a wavelength of 1150 nm. This was achieved by using low-temperature solution processing methods for the active layer, which could enable lower cost devices on a wide variety of substrates. Devices showed responsivity up to 1400 nm, significantly broader than comparable materials such as $CuInSe_2$. This combination of good material processability and device performance demonstrates that Ag_2Se CQDs offer a low-toxicity route for low-cost fabrication of NIR-II photodiodes.

EXPERIMENTAL METHODS

Ag_2Se Quantum Dot Synthesis and Characterization. All chemicals were purchased from Sigma-Aldrich (unless otherwise specified): silver acetate (AgAc, 99.99%), selenium (Se, 100 mesh, 99.99%), 1-dodecanethiol (DDT, ≥98%), 1-octadecene (ODE, 90%), tri-*n*-octylphosphine (TOP, 90%), diphenylphosphine (DPP, 98%), tetrachloroethylene (TCE, 99%, spectrophotometric grade), 1,2-dichloroethane (99.8%), and dye IR 26 (Exciton). The solvents used for purification were toluene (99.5%, ACS reagent, ACP in Montreal), ethanol (anhydrous), and methanol (absolute, ACP in Montreal).

Standard air-free techniques were used during the synthesis. In small scale syntheses as shown in Figure 2, 34 mg (0.2 mmol) of AgAC, 0.4 mL of DDT, and 5.0 mL of ODE were mixed in a three-necked 50 mL round-bottomed flask equipped with an air condenser and a thermometer. The mixture was heated at 70 °C in a vacuum (50 mTorr) for 90 min. Afterward, the mixture was purged with high-purity nitrogen and then heated to the desired injection temperature. In a glovebox filled by nitrogen, a 0.1 M TOPSe stock solution was prepared by stirring Se in TOP (purity 90%) until all dissolved. 1.0 mL of TOPSe (0.1 mmol) and 8 μL of DPP were mixed and loaded in a syringe, which was then swiftly injected into the flask at 140 °C, followed by 60 min growth at 120 °C, with sampling at 3, 10, 20, 30,

https://dx.doi.org/10.1021/acsanm.0c02686
ACS Appl. Nano Mater. 2020, 3, 12209–12217

45, and 60 min. In the upscaling synthesis, 448 mg (2.68 mmol) of AgAc, 2.0 mL of DDT, and 25 mL of ODE were mixed in a three-necked 100 mL flask. In a glovebox filled by nitrogen, 1.0 M TOPSe stock solution was prepared by stirring Se in TOP (90%) until all dissolved. 1.25 mL of TOPSe (1.25 mmol), 109 μL of DPP, and 4.0 mL of TOP (purity 90%) were mixed and loaded in a syringe, which was then swiftly injected into the flask at 140 °C, followed by 60 min growth at 120 °C. The growth was quenched by fast cooling using pressured air. The crude product was stored in a freezer at −30 °C overnight to allow completion of possible crystal structure conversion. The purification was done by dispersing the crude product in toluene, followed by precipitation by adding anhydrous ethanol and centrifugation. After 30 min centrifugation at 9000 rpm, the precipitated QDs from the upscaling synthesis were further purified up to five times in total. The precipitated QDs were dispersed in toluene and centrifuged at 5000 rpm for 10 min to remove possible aggregated QDs in the middle of purification. The purified product was dried by using nitrogen blowing and stored in a nitrogen-filled glovebox.

Ultraviolet−visible−near-IR (UV−vis−NIR) absorption spectra were collected by using a 1 nm data interval (Varian Cary 5000 spectrophotometer). Near-IR PL emission spectra were collected with a Horiba Jobin Yvon Fluorolog-3 model FL3-11 spectrofluorometer, equipped with a 2 mm diameter InGaAs photodiode which was operated at room temperature. Both the entrance and exit slits were 5 nm, and the data increment was 1 nm. Dilute purified Ag_2Se QD dispersion in TCE was used. The PL QY was estimated by comparing the sample emission intensity with that of IR26 dye in 1,2-dichloroethane (lit. QY 0.5%). Corrections were made for the difference of the refractive index of the two solvents. The TEM sample was prepared by depositing dilute purified Ag_2Se dispersion in hexane onto a 400-mesh thin-carbon-coated copper grid. TEM images were collected on a JEOL JEM-2100F electron microscope operating at 200 kV and equipped with a Gatan UltraScan 1000 CCD camera. The QD size and standard deviation were obtained by analyzing ∼200 individual Ag_2Se QDs. Energy-dispersive X-ray spectroscopy (EDX) was done in the STEM mode by using an Oxford INCA Energy TEM 200 attached to the JEM-2100F, and the EDX sample was prepared by depositing concentrated purified Ag_2Se dispersion in hexane on a copper grid. SEM images of the device cross section created by focused ion beam were collected on a Hitachi field-emission SU5000 scanning electron microscope.

Photodetector Fabrication and Characterization. Devices were fabricated on glass, with prepatterned FTO electrodes commercially purchased. Substrates were cleaned by rinsing in DI water and acetone, prior to UV-ozone treatment for 10 min. A thin (∼30 nm) TiO_2 layer (Ti-Nanoxide BL/SC, Solaronix) was deposited by using spin coating (5000 rpm, 30 s), followed by sintering for 30 min at 550 °C. The mesoporous TiO_2 layer (∼600 nm, Ti-Nanoxide T600/SC, Solaronix) was then deposited by using spin coating (5000 rpm, 30 s), followed by sintering for 1 h at 475 °C. Ag_2Se QDs were then deposited by using a ligand exchange process. The Ag_2Se QDs were dispersed in toluene at a concentration of 8 mg/mL. This solution was then drop-cast onto the mesoporous TiO_2 layer and left to stand for 1 min to allow diffusion into the mesoporous structure. Excess solution was removed by spinning the sample at 800 rpm for 1 min before immersing the sample in a bath of acetonitrile + 0.02 M 1,3-benzenedithiol for 1 min. Samples were then rinsed in a bath of acetonitrile and dried before repeating the process as required. Up to 17 layers of Ag_2Se QDs were fabricated. All Ag_2Se deposition was performed in an inert atmosphere. To aid hole transport in some devices, a HTL of doped Spiro-OMeTAD was drop-cast onto the sample and left to stand for 1 min before removal of excess by spinning (500 rpm, 1 min). The HTL solution was prepared by dissolving 145 mg of (2,2′,7,7′-tetrakis(*N*,*N*-di-*p*-methoxyphenylamine)-9,9′-spirobifluorene) (Spiro-OMeTAD) in 2 mL of chlorobenzene, followed by the addition of 58 μL of 4-*tert*-butylpyridine and 35 μL of 520 mg mL^{-1} lithium bis(trifluoromethylsulfonyl)imide (Li-TFSI)−acetonitrile solution. Finally, a 100 nm thick silver electrode was deposited by thermal evaporation through a shadow mask to define the active area of photodetectors (0.49 cm^2).

EQE measurements were performed in air by using a Jobin-Yvon Triax spectrometer, a Jobin-Yvon xenon light source, a Merlin lock-in amplifier, a calibrated Ge detector from Newport, and an SR570 low noise current amplifier. The responsivity at 1200 nm was measured by using a supercontinuum laser source model SC-5 from YSL Photonics. The narrow band at 1200 nm was obtained by passing through an IR (1200 nm, OD 4) 25 nm band-pass filter from Edmund Optics. The optical intensity can be adjusted by the output control on laser source or OD 25 mm diameter NIR ND filter from Edmund Optics, which were further calibrated by a Newport power meter model 1918-C coupled with a photodiode sensor (918D-IG-OD1).

■ ASSOCIATED CONTENT

Supporting Information

The Supporting Information is available free of charge at https://pubs.acs.org/doi/10.1021/acsanm.0c02686.

Ag_2Se QDs TEM images, size histogram, EDX measurements, TGA curve, and ligand density calculation, FT-IR spectrum, XPS spectra, and absorption spectrum of a cross-linked Ag_2Se QD film (PDF)

■ AUTHOR INFORMATION

Corresponding Authors

Jianping Lu − *Advanced Electronics and Photonics Research Centre, National Research Council of Canada, Ottawa, ON, Canada K1A 0R6*; orcid.org/0000-0003-3152-7510; Email: jianping.lu@nrc-cnrc.gc.ca

Ye Tao − *Advanced Electronics and Photonics Research Centre, National Research Council of Canada, Ottawa, ON, Canada K1A 0R6*; Email: ye.tao@nrc-cnrc.gc.ca

Authors

Neil Graddage − *Advanced Electronics and Photonics Research Centre, National Research Council of Canada, Ottawa, ON, Canada K1A 0R6*

Jianying Ouyang − *Security and Disruptive Technologies Research Centre, National Research Council of Canada, Ottawa, ON, Canada K1A 0R6*

Ta-Ya Chu − *Advanced Electronics and Photonics Research Centre, National Research Council of Canada, Ottawa, ON, Canada K1A 0R6*

Yanguang Zhang − *Advanced Electronics and Photonics Research Centre, National Research Council of Canada, Ottawa, ON, Canada K1A 0R6*

Zhao Li − *Security and Disruptive Technologies Research Centre, National Research Council of Canada, Ottawa, ON, Canada K1A 0R6*

Xiaohua Wu − *Advanced Electronics and Photonics Research Centre, National Research Council of Canada, Ottawa, ON, Canada K1A 0R6*

Patrick R. L. Malenfant − *Security and Disruptive Technologies Research Centre, National Research Council of Canada, Ottawa, ON, Canada K1A 0R6*; orcid.org/0000-0001-5391-2300

Complete contact information is available at: https://pubs.acs.org/10.1021/acsanm.0c02686

Author Contributions

N.G. and J.O. contributed equally to this work.

Notes

The authors declare no competing financial interest.

https://dx.doi.org/10.1021/acsanm.0c02686
ACS Appl. Nano Mater. 2020, 3, 12209−12217

■ ACKNOWLEDGMENTS

The authors thank Mr. Hiroshi Fukutani, Ms. Simona Moisa, Mr. Oltion Kodra, Ms. Mary Gallerneault, and Dr. Stephen Lang at NRC for their technical support. We also thank Dr. Simon King at Cambridge Display Technology for fruitful discussions. The financial support from Cambridge Display Technology, UK, and National Research Council Canada is greatly acknowledged.

■ REFERENCES

(1) Liu, H.; Boas, D. A.; Zhang, Y.; Yodh, A. G.; Chance, B. Determination of Optical Properties and Blood Oxygenation in Tissue Using Continuous NIR Light. *Phys. Med. Biol.* **1995**, *40*, 1983−1993.

(2) Park, S.; Fukuda, K.; Wang, M.; Lee, C.; Yokota, T.; Jin, H.; Jinno, H.; Kimura, H.; Zalar, P.; Matsuhisa, N.; Umezu, S.; Bazan, G. C.; Someya, T. Ultraflexible Near-Infrared Organic Photodetectors for Conformal Photoplethysmogram Sensors. *Adv. Mater.* **2018**, *30*, 1802359.

(3) Tamura, T.; Maeda, Y.; Sekine, M.; Yoshida, M. Wearable Photoplethysmographic Sensors—Past and Present. *Electronics* **2014**, *3*, 282−302.

(4) Rogalski, A. Infrared Detectors: Status and Trends. *Prog. Quantum Electron.* **2003**, *27*, 59−210.

(5) Guyot-Sionnest, P.; Ackerman, M. M.; Tang, X. Colloidal Quantum Dots for Infrared Detection Beyond Silicon. *J. Chem. Phys.* **2019**, *151*, 060901.

(6) Konstantatos, G.; Howard, I.; Fischer, A.; Hoogland, S.; Clifford, J.; Klem, E.; Levina, L.; Sargent, E. H. Ultrasensitive Solution-Cast Quantum Dot Photodetectors. *Nature* **2006**, *442*, 180−183.

(7) Sun, B.; Ouellette, O.; de Arquer, F. P. G.; Voznyy, O.; Kim, Y.; Wei, M.; Proppe, A. H.; Saidaminov, M. I.; Xu, J.; Liu, M.; Li, P.; Fan, J. Z.; Jo, J. W.; Tan, H.; Tan, F.; Hoogland, S.; Lu, Z. H.; Kelley, S. O.; Sargent, E. H. Multibandgap Quantum Dot Ensembles for Solar-Matched Infrared Energy Harvesting. *Nat. Commun.* **2018**, *9*, 4003.

(8) Ip, A. H.; Thon, S. M.; Hoogland, S.; Voznyy, O.; Zhitomirsky, D.; Debnath, R.; Levina, L.; Rollny, L. R.; Carey, G. H.; Fischer, A.; Kemp, K. W.; Kramer, I. J.; Ning, Z.; Labelle, A. J.; Chou, K. W.; Amassian, A.; Sargent, E. H. Hybrid Passivated Colloidal Quantum Dot Solids. *Nat. Nanotechnol.* **2012**, *7*, 577−582.

(9) Böberl, M.; Kovalenko, M. V.; Gamerith, S.; List, E. J. W.; Heiss, W. Inkjet-Printed Nanocrystal Photodetectors Operating up to 3 μm Wavelengths. *Adv. Mater.* **2007**, *19*, 3574−3578.

(10) Xiao, X.; Xu, K.; Yin, M.; Qiu, Y.; Zhou, W.; Zheng, L.; Cheng, X.; Yu, Y.; Ning, Z. High quality silicon: Colloidal Quantum Dot Heterojunction Based Infrared Photodetector. *Appl. Phys. Lett.* **2020**, *116*, 101102.

(11) Xu, K.; Xiao, X.; Zhou, W.; Jiang, X.; Wei, Q.; Chen, H.; Deng, Z.; Huang, J.; Chen, B.; Ning, Z. Inverted Si:PbS Colloidal Quantum Dot Heterojunction-Based Infrared Photodetector. *ACS Appl. Mater. Interfaces* **2020**, *12*, 15414−15421.

(12) Urban, J. J.; Talapin, D. V.; Shevchenko, E. V.; Kagan, C. R.; Murray, C. B. Synergism in Binary Nanocrystal Superlattices Leads to Enhanced p-Type Conductivity in Self-Assembled PbTe/Ag_2Te Thin Films. *Nat. Mater.* **2007**, *6*, 115−121.

(13) Yarema, M.; Pichler, S.; Sytnyk, M.; Seyrkammer, R.; Lechner, R. T.; Fritz-Popovski, G.; Jarzab, D.; Szendrei, K.; Resel, R.; Korovyanko, O.; Loi, M. A.; Paris, O.; Hesser, G.; Heiss, W. Infrared Emitting and Photoconducting Colloidal Silver Chalcogenide Nanocrystal Quantum Dots from a Silylamide-Promoted Synthesis. *ACS Nano* **2011**, *5*, 3758−3765.

(14) Qu, J.; Goubet, N.; Livache, C.; Martinez, B.; Amelot, D.; Gréboval, C.; Chu, A.; Ramade, J.; Cruguel, H.; Ithurria, S.; Silly, M. G.; Lhuillier, E. Intraband Mid-Infrared Transitions in Ag_2Se Nanocrystals: Potential and Limitations for Hg-Free Low-Cost Photodetection. *J. Phys. Chem. C* **2018**, *122*, 18161−18167.

(15) Hafiz, S. B.; Scimeca, M. R.; Zhao, P.; Paredes, I. J.; Sahu, A.; Ko, D.-K. Silver Selenide Colloidal Quantum Dots for Mid-Wavelength Infrared Photodetection. *ACS Appl. Nano Mater.* **2019**, *2*, 1631−1636.

(16) Park, M.; Choi, D.; Choi, Y.; Shin, H.-b.; Jeong, K. S. Mid-Infrared Intraband Transition of Metal Excess Colloidal Ag_2Se Nanocrystals. *ACS Photonics* **2018**, *5*, 1907−1911.

(17) Lee, W.-Y.; Ha, S.; Lee, H.; Bae, J.-H.; Jang, B.; Kwon, H.-J.; Yun, Y.; Lee, S.; Jang, J. High-Detectivity Flexible Near-Infrared Photodetector Based on Chalcogenide Ag_2Se Nanoparticles. *Adv. Opt. Mater.* **2019**, *7*, 1900812.

(18) Li, N.; Lan, Z.; Cai, L.; Zhu, F. Advances in Solution-Processable Near-Infrared Phototransistors. *J. Mater. Chem. C* **2019**, *7*, 3711−3729.

(19) Iacovo, A. D.; Venettacci, C.; Colace, L.; Scopa, L.; Foglia, S. PbS Colloidal Quantum Dot Photodetectors Operating in the Near Infrared. *Sci. Rep.* **2016**, *6*, 37913.

(20) Yang, Y.; Pan, D.; Zhang, Z.; Chen, T.; Xie, H.; Gao, J.; Guo, X. Ag_2Se Quantum Dots for Photovoltaic Applications and Ligand Effects on Device Performance. *J. Alloys Compd.* **2018**, *766*, 925−932.

(21) Guo, R.; Shen, T.; Tian, J. Broadband Hybrid Organic/CuInSe2 Quantum Dot Photodetectors. *J. Mater. Chem. C* **2018**, *6*, 2573−2579.

(22) Hsu, C.-Y.; Chen, Y.-C.; Lin, R. Y.-Y.; Ho, K.-C.; Lin, J. T. Solid-State Dye-Sensitized Solar Cells Based on Spirofluorene (spiro-OMeTAD) and Arylamines as Hole Transporting Materials. *Phys. Chem. Chem. Phys.* **2012**, *14*, 14099−14109.

(23) Casalino, M.; Coppola, G.; Iodice, M.; Rendina, I.; Sirleto, L. Near-Infrared Sub-Bandgap All-Silicon Photodetectors: State of the Art and Perspectives. *Sensors* **2010**, *10*, 10571−10600.

(24) Sahu, A.; Qi, L.; Kang, M. S.; Deng, D.; Norris, D. J. Facile Synthesis of Silver Chalcogenide (Ag_2E; E = Se, S, Te) Semiconductor Nanocrystals. *J. Am. Chem. Soc.* **2011**, *133*, 6509−6512.

(25) Sahu, A.; Khare, A.; Deng, D. D.; Norris, D. J. Quantum Confinement in Silver Selenide Semiconductor Nanocrystals. *Chem. Commun.* **2012**, *48*, 5458−5460.

(26) Zhu, C.-N.; Jiang, P.; Zhang, Z.-L.; Zhu, D.-L.; Tian, Z.-Q.; Pang, D.-W. Ag2Se Quantum Dots with Tunable Emission in the Second Near-Infrared Window. *ACS Appl. Mater. Interfaces* **2013**, *5*, 1186−1189.

(27) Shi, L.-J.; Zhu, C.-N.; He, H.; Zhu, D.-L.; Zhang, Z.-L.; Pang, D.-W.; Tian, Z.-Q. Near-Infrared Ag_2Se Quantum Dots with Distinct Absorption Features and high Fluorescence Quantum Yields. *RSC Adv.* **2016**, *6*, 38183−38186.

(28) Evans, C. M.; Evans, M. E.; Krauss, T. D. Mysteries of TOPSe Revealed: Insights into Quantum Dot Nucleation. *J. Am. Chem. Soc.* **2010**, *132*, 10973−10975.

(29) Ouyang, J.; Schuurmans, C.; Zhang, Y.; Nagelkerke, R.; Wu, X.; Kingston, D.; Wang, Z. Y.; Wilkinson, D.; Li, C.; Leek, D. M.; Tao, Y.; Yu, K. Low-Temperature Approach to High-Yield and Reproducible Syntheses of High-Quality Small-Sized PbSe Colloidal Nanocrystals for Photovoltaic Applications. *ACS Appl. Mater. Interfaces* **2011**, *3*, 553−565.

(30) Yu, K.; Ouyang, J.; Zhang, Y.; Tung, H.-T.; Lin, S.; Nagelkerke, R. A. L.; Kingston, D.; Wu, X.; Leek, D. M.; Wilkinson, D.; Li, C.; Chen, I.-G.; Tao, Y. Low-Temperature Noninjection Approach to Homogeneously-Alloyed $PbSe_xS_{1-x}$ Colloidal Nanocrystals for Photovoltaic Applications. *ACS Appl. Mater. Interfaces* **2011**, *3*, 1511−1520.

(31) Yu, K.; Hrdina, A.; Zhang, X.; Ouyang, J.; Leek, D. M.; Wu, X.; Gong, M.; Wilkinson, D.; Li, C. Highly-Photoluminescent ZnSe Nanocrystals via a Non-Injection-Based Approach with Precursor Reactivity Elevated by a Secondary Phosphine. *Chem. Commun.* **2011**, *47*, 8811−8813.

(32) Yu, K.; Ng, P.; Ouyang, J.; Zaman, M. B.; Abulrob, A.; Baral, T. N.; Fatehi, D.; Jakubek, Z. J.; Kingston, D.; Wu, X.; Liu, X.; Hebert, C.; Leek, D. M.; Whitfield, D. M. Low-Temperature Approach to Highly Emissive Copper Indium Sulfide Colloidal Nanocrystals and Their Bioimaging Applications. *ACS Appl. Mater. Interfaces* **2013**, *5*, 2870−2880.

(33) Yu, K.; Liu, X.; Zeng, Q.; Leek, D. M.; Ouyang, J.; Whitmore, K. M.; Ripmeester, J. A.; Tao, Y.; Yang, M. Effect of Tertiary and

https://dx.doi.org/10.1021/acsanm.0c02686
ACS Appl. Nano Mater. 2020, 3, 12209−12217

Secondary Phosphines on Low-Temperature Formation of Quantum Dots. *Angew. Chem., Int. Ed.* **2013**, *52*, 4823−4828.
(34) Yu, K.; Liu, X.; Zeng, Q.; Yang, M.; Ouyang, J.; Wang, X.; Tao, Y. The Formation Mechanism of Binary Semiconductor Nanomaterials: Shared by Single-Source and Dual-Source Precursor Approaches. *Angew. Chem., Int. Ed.* **2013**, *52*, 11034−11039.
(35) Ouyang, J.; Zhang, Y.; Lu, J.; Chu, T.-Y.; Graddage, N.; Malenfant, P.; Tao, Y. Synthesis of Monodisperse Silver Chalcogenide Quantum Dots with Elevated Precursor Reactivity for the Application in Near Infrared Photodetectors. 2019 IEEE International Flexible Electronics Technology Conference (IFETC), Vancouver, Canada, 2019; pp 1−2.
(36) Ji, C.; Zhang, Y.; Zhang, T.; Liu, W.; Zhang, X.; Shen, H.; Wang, Y.; Gao, W.; Wang, Y.; Zhao, J.; Yu, W. W. Temperature-Dependent Photoluminescence of Ag_2Se Quantum Dots. *J. Phys. Chem. C* **2015**, *119*, 13841−13846.
(37) Fisher, A. A. E.; Osborne, M. A.; Day, I. J.; Alcalde, G. L. Measurement of Ligand Coverage on Cadmium Selenide Nanocrystals and its Influence on Dielectric Dependent Photoluminescence Intermittency. *Commun. Chem.* **2019**, 63.
(38) Sahu, A.; Braga, D.; Waser, O.; Kang, M. S.; Deng, D.; Norris, D. J. Solid-Phase Flexibility in Ag_2Se Semiconductor Nanocrystals. *Nano Lett.* **2014**, *14*, 115−121.
(39) Wang, J.; Fan, W.; Yang, J.; Da, Z.; Yang, X.; Chen, K.; Yu, H.; Cheng, X. Tetragonal−Orthorhombic−Cubic Phase Transitions in Ag_2Se Nanocrystals. *Chem. Mater.* **2014**, *26*, 5647−5653.
(40) Kobayashi, M. Review on Structural and Dynamical Properties of Silver Chalcogenides. *Solid State Ionics* **1990**, *39*, 121−149.
(41) Fu, H.; Tsang, S.-W.; Zhang, Y.; Ouyang, J.; Lu, J.; Yu, K.; Tao, Y. Impact of the Growth Conditions of Colloidal PbS Nanocrystals on Photovoltaic Device Performance. *Chem. Mater.* **2011**, *23*, 1805−1810.
(42) Lim, K. H.; Wong, K. W.; Liu, Y.; Zhang, Y.; Cadavid, D.; Cabot, A.; Ng, K. M. Critical Role of Nanoinclusions in Silver Selenide Nanocomposites as a Promising Room Temperature Thermoelectric Material. *J. Mater. Chem. C* **2019**, *7*, 2646−2652.
(43) Abate, A.; Leijtens, T.; Pathak, S.; Teuscher, J.; Avolio, R.; Errico, M. E.; Kirkpatrik, J.; Ball, J. M.; Docampo, P.; McPherson, I.; Snaith, H. J. Lithium Salts as "Redox Active" p-Type Dopants for Organic Semiconductors and their Impact in Solid-State Dye-Sensitized Solar Cells. *Phys. Chem. Chem. Phys.* **2013**, *15*, 2572−2579.
(44) Namespetra, A. M.; Hendsbee, A. D.; Welch, G. C.; Hill, I. G. Development of Simple Hole-Transporting Materials for Perovskite Solar Cells. *Can. J. Chem.* **2016**, *94*, 352−359.
(45) Hawash, Z.; Ono, L. K.; Qi, Y. Moisture and Oxygen Enhance Conductivity of LiTFSI-Doped Spiro-MeOTAD Hole Transport Layer in Perovskite Solar Cells. *Adv. Mater. Interfaces* **2016**, *3*, 1600117.

https://dx.doi.org/10.1021/acsanm.0c02686
ACS Appl. Nano Mater. 2020, 3, 12209−12217